ISSN 0020-1685, Inorganic Materials, 2016, Vol. 52, No. 7, pp. 721–728. © Pleiades Publishing, Ltd., 2016.
Original Russian Text © E.V. Dedyaeva, P.N. Nikiforov, A.G. Padalko, G.V. Talanova, L.I. Shvorneva, 2016, published in Neorganicheskie Materialy, 2016, Vol. 52, No. 7, pp. 778–786.

Effect of Barothermal Processing on the Microstructure and Properties of Al–10 at % Si Hypoeutectic Binary Alloy

E. V. Dedyaeva[a], P. N. Nikiforov[b], A. G. Padalko[a], G. V. Talanova[a], and L. I. Shvorneva[a]

[a] *Baikov Institute of Metallurgy and Materials Science, Russian Academy of Sciences, Leninskii pr. 49, Moscow, 119991 Russia*

[b] *Ufa Engine Industrial Association Public Joint Stock Company, ul. Ferina 2, Ufa, 450039 Russia*

e-mail: padalko@inbox.ru

Received September 21, 2015

Abstract—We describe barothermal processing (hot isostatic pressing) of an Al–10 at % Si binary alloy for 3 h at a temperature of 560°C and pressure of 100 MPa. The results demonstrate that this processing ensures a high degree of homogenization of the as-prepared alloy, which is chemically and structurally inhomogeneous. The morphology of the silicon microparticles in the material suggests that heat treatment of the Al–10 at % Si alloy at 560°C and a pressure of 100 MPa leads to a thermodynamically driven, essentially complete silicon dissolution in the aluminum matrix and the formation of a metastable, supersaturated solid solution, which subsequently decomposes during cooling. We analyze the associated porosity elimination process, which makes it possible to obtain a material with 100% relative density. Barothermal processing of the Al–10 at % Si alloy is shown to produce a bimodal size distribution of the silicon phase constituent: microparticles 1.6 μm in average size and nanoparticles 43 nm in average size. Barothermal processing is shown to reduce the thermal expansion coefficient of the alloy, and the microhardness of the two-phase alloy is determined. Based on the present results, we conclude that barothermal processing is an effective tool for eliminating microporosity from the Al–10 at % Si alloy, reaching a high degree of homogenization, and producing a near-optimal microstructure, which surpasses results of conventional heat treatment of the material at atmospheric and reduced pressures.

Keywords: silumin, microstructure, hot isostatic pressing, silicon dissolution, diffusion

DOI: 10.1134/S0020168516070049

INTRODUCTION

Aluminum alloys are widely used in modern technology to produce structural materials with low density, high corrosion resistance, and rather good mechanical properties. Alloys based on the simple eutectic binary system Al–Si constitute a considerable fraction of the aluminum-based metallic materials. Since a large amount of reliable experimental data obtained in physicochemical studies was used to construct the equilibrium phase diagram of this system [1], it is considered canonical [2, 3]. The system is attractive for barothermal experiments owing to its simplicity. In particular, there is no chemical interaction between the components of the alloy over the entire composition range. Its phase diagram has a rather wide range of solid solutions of silicon in aluminum (Al), with a solubility limit of 1.6 at % Si at the eutectic temperature (577°C, 12.2 at % Si). In addition, the binary alloys of the Al–Si system have the advantages of being easy to synthesize, having relatively low phase transformation temperatures, being composed of components with low saturated vapor pressure, and being nonreactive with typical crucible materials, which allows these alloys to be employed as model systems for gaining insight into barothermal processing (BTP) mechanisms.

Cast aluminum alloys based on the basic binary system Al–Si (silumins) constitute a large group of materials whose compositions lie mainly in the aluminum-rich, hypoeutectic region, at silicon concentrations $7 \leqslant C_{Si} < 12$ at %, and several alloys with the eutectic composition and hypereutectic silicon concentrations, $12 \leqslant C_{Si} \leqslant 13$ at %. To improve their mechanical properties, cast silumins are heat-treated with the aim of reducing the cooling-induced stress in the cast alloys and improving the morphology of silicon inclusions, which contain a coarse needle-like (Al) + Si eutectic [4], unfavorable for the mechanical properties of the alloys.

Like many other alloys, cast alloys based on the Al–Si system possess shrinkage porosity resulting from changes in the specific volumes of the liquid and solid phases during solidification. When silumins are employed in highly loaded parts, porosity is eliminated by hot isostatic pressing (HIP) [5, 6]. Heating a material in order to reduce its yield strength, in combination with uniform pressure, makes it possible to considerably raise the density of the material, often to

its theoretical density, thereby improving its mechanical and engineering characteristics [6]. Note that HIP is most effective when it is used to eliminate porosity in both metallic [7] and ceramic [8] materials. This technique relies, on the one hand, on a theoretical basis that allows one to model HIP densification processes [9–11] and, on the other, on experimental studies [12, 13] in this area of research. A number of studies have been concentrated on the HIP processing of aluminum alloys for the fabrication of high-density materials [14, 15].

At the same time, there has been much less work on phenomena related to BTP-induced changes in the morphology of structural constituents of alloys. It is worth noting that many metallic materials are subjected to high pressures in a temperature range near temperatures of conventional heat treatment. In the case of an appropriate choice of the temperature range and cooling rate, conventional solid-state heat treatment of materials improves the chemical homogeneity of alloys and ensures advantageous changes in the morphology of the structural constituents of the alloy by diffusion mechanisms. Similar results would be expected in the case of BTP, but in the literature concerned with HIP such studies, for example, for materials that are used in turbine blades (high-temperature nickel and titanium alloys) and for aluminum alloys, in particular, for the Al–10Si binary silumin (here and in what follows, alloy compositions are expressed as an atomic percent), are deficient. Since the microstructure of metallic materials plays a key role in determining their properties, microstructure formation in metallic materials at high pressures and temperatures requires detailed investigation with the use of various physicochemical characterization techniques.

In connection with this, the purpose of this work was to assess the effect of barothermal processing on microstructure formation in Al–10Si silumin and find correlation relationships with some mechanical properties of the alloy.

EXPERIMENTAL

Al–10Si alloy samples for this investigation were synthesized using PA-1 aluminum powder (⩾99% Al) with a particle size under 100 μm and Kr00 silicon powder (⩾99% Si) with a similar particle size composition. Ingots were prepared by vacuum suction using a Kristall-702 inductively heated system in flowing argon. The powders were melted and the melt was heated to 700°C in a quartz crucible. After complete silicon dissolution in the aluminum, a quartz tube 3.6 mm in inner diameter was immersed vertically in the melt. After the pressure in the tube was sharply reduced relative to that in the melt, the liquid metal filled the tube to a height of ≃100 mm. Under these conditions, the melt was then cooled at a rate on the order of tens of degrees Celsius, with supercooling. These synthesis conditions resulted in multinuclei crystallization and the formation of samples with a microcrystalline structure and a rather uniform distribution of the structural components of the alloy: aluminum and silicon.

BTP was carried out in an HIRP 20-70-200-2000 apparatus (ABRA, Switzerland) in an argon atmosphere using a system of graphite heaters. After the samples were placed in the working chamber, the pressure was raised to ≃53 MPa and then the temperature was raised at a constant rate of 10°C/min to an isobaric–isothermal holding temperature. At this temperature, the pressure reached 100 ± 2 MPa. This temperature was maintained with an accuracy of ±1°C throughout the holding time. After the barothermal processing cycle, the samples were cooled to 300°C at a rate of 7°C/min and then to room temperature at a higher rate.

Samples for characterization, 3.6 mm in diameter and ≃10 mm in length, were cut with a diamond saw blade on a Discotom cut-off machine (Struers, Germany). Polished sections for microstructural analysis were prepared using diamond pastes, electrolytic polishing, and chemical etching in a selective etchant. Microstructures were examined first on an MeF3 optical microscope (Austria) equipped with a digital imaging accessory. Higher resolution images were obtained by scanning electron microscopy (SEM) on a TESCAN VEGA SBU II instrument (Czechia). Images were typically obtained in backscatter mode at an accelerating voltage of 20 kV, as well as in characteristic SiK_α X-rays. X-ray diffraction measurements were made on a Shimadzu XRD-6000 diffractometer (Japan) with CuK_α radiation (λ = 1.5406 Å). Vickers microhardness tests were performed on a PMT-3 microhardness tester (OAO LOMO, Russia) by a standard procedure. Quantitative information about the microstructural constituents of the alloy was obtained by processing and analyzing images with AdobePhotoshop CS6 and ImageJ, respectively. Histograms and curves were constructed with Origin 5.0 software.

The linear thermal expansion of the samples was measured on a DIL 402 C dilatometer equipped with a vacuum furnace (Netzsch, Germany). Using simple calculations, the temperature dependences of the relative length change were converted into temperature dependences of the thermal expansion coefficient (TEC).

RESULTS AND DISCUSSION

The microstructure of the as-prepared alloy (Fig. 1a) consisted of primary aluminum dendrites, with first- and second-order axes up to 10–40 μm in length, and an (Al) + Si eutectic, where the silicon had the form of small rounded precipitates with characteristic dimensions on the order of several microns, which formed an essentially continuous silicon skeleton in the interdendrite spaces of the primary aluminum crystals.

The synthesized as-prepared alloy had considerable porosity, localized in the α-matrix, whereas the eutectic silicon particles were free of such structural defects. By analyzing optical microscopy images with the use of appropriate software, we obtained a histogram of the pore size distribution (Fig. 1b) and quantitative data on the porosity of the as-prepared material. In particular, the pore volume fraction in the (Al) solid solution was 7.0 vol % as determined proceeding from quantitative metallography concepts [16], the pore number density was 8.3×10^{10} cm^{-3}, the average center-to-center pore distance was 2.2 μm, the average pore diameter was 0.68 μm, and the average pore volume was 1.6×10^{-13} cm^3. The reason for the increased porosity of the as-prepared material was that the alloy was synthesized from powders. Since the aluminum and silicon particles had surface oxide films, this led to pore formation. An analytical relation between the number of pores and their diameter has the form

$$N^0_{\text{pores}} = 5.2\times10^1 e^{-5.6d},$$

where N^0_{pores} is the number of pores in the as-prepared material and d (μm) is the pore diameter.

The BTP temperature was chosen using differential barothermal analysis (DBA) data for the Al–10Si alloy [17]. According to previous DBA data, heating the Al–10Si alloy to a temperature near 553°C at a uniform argon pressure p = 100 MPa led to solid-state silicon dissolution, and subsequent cooling led to silicon precipitation as a result of the decomposition of the supersaturated (Al) solid solution. Some of the resultant silicon particles were submicron-sized [17]. Based on those results, small ingots 3.6 mm in diameter and 10 mm in length were subjected to BTP for 3 h at an isobaric–isothermal holding temperature of 560 ± 1°C, which was ≃7°C above the solid-state transformation temperature according to DBA data.

SEM examination showed that the alloy underwent significant changes (Fig. 2a). First, the as-prepared, porous alloy acquired a complete density, as was expected. Microstructural defects in the form of pores in the (Al) solid solution were detected at none of the magnifications used in optical microscopy or SEM (in the latter instance, backscattered electron images were obtained at magnifications of up to 60000×). This result is sufficiently obvious because the applied uniform pressure of 100 MPa considerably exceeds the yield strength of the alloy containing 0.72 wt % silicon: ≃10 MPa at a temperature of 500°C, as determined from uniaxial compression results obtained in the temperature range 30–500°C [22]. When extrapolating the data obtained by Schumacher et al. [22] to the higher temperatures used in our BTP cycles, it is reasonable to expect a decrease in the yield strength of the Al–10Si alloy at 560°C to a few megapascals. The applied uniform pressure of 100 MPa is then many times higher than the yield strength of the alloy and plays a key role in determining active plastic deformation of the pores, subsequent closure of their walls, and diffusion joining of the surfaces brought into contact. In analyzing the diffusion joining process, we proceeded from the temperature dependence obtained by Fujikawa et al. [18] for the self-diffusion coefficient of aluminum atoms under ordinary conditions and assumed that, at the pressure of 100 MPa used in this study, only a slight pressure-induced decrease in aluminum self-diffusion coefficient is possible, by analogy with previous results on the influence of pressure on diffusion coefficients in high-temperature nickel alloys ($D^{150\text{MPa}} \simeq 0.9D^{0.1\text{MPa}}$) [20]:

$$D_{\text{Al/Al}} = 5.07\times10^{-4}\exp\left(-143\ \frac{\text{kJ}}{\text{mol}}\Big/RT\right), \qquad (1)$$

where $D_{\text{Al/Al}}$ (m^2/s) is the aluminum self-diffusion coefficient, R (J/(mol K)) is the gas constant, and T (K) is the absolute temperature.

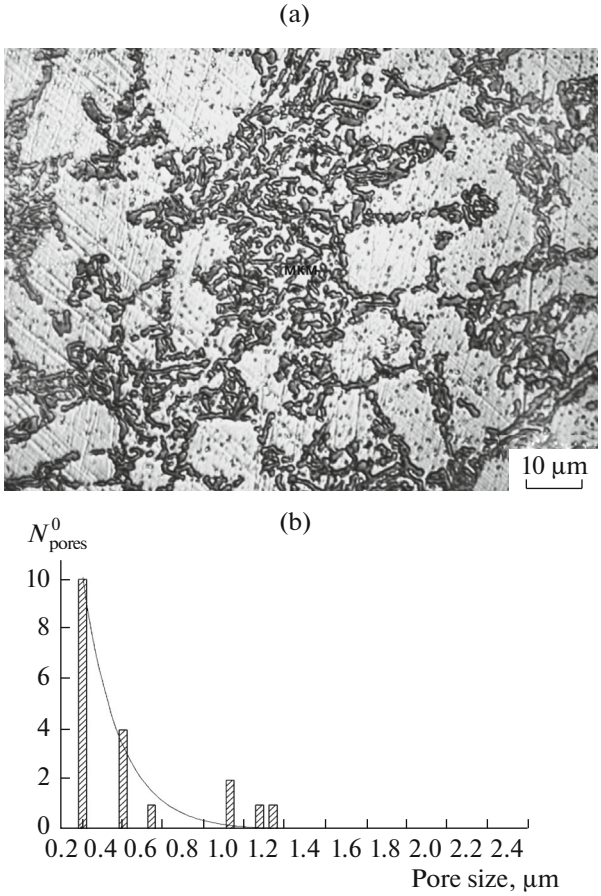

Fig. 1. (a) Microstructure of the as-prepared Al–10Si alloy (optical microscopy, magnification of 1000×), consisting of primary aluminum dendrites (light areas), an (Al) + Si eutectic, and pores in the primary aluminum crystals; (b) histogram of the pore size distribution in the aluminum matrix of the as-prepared alloy.

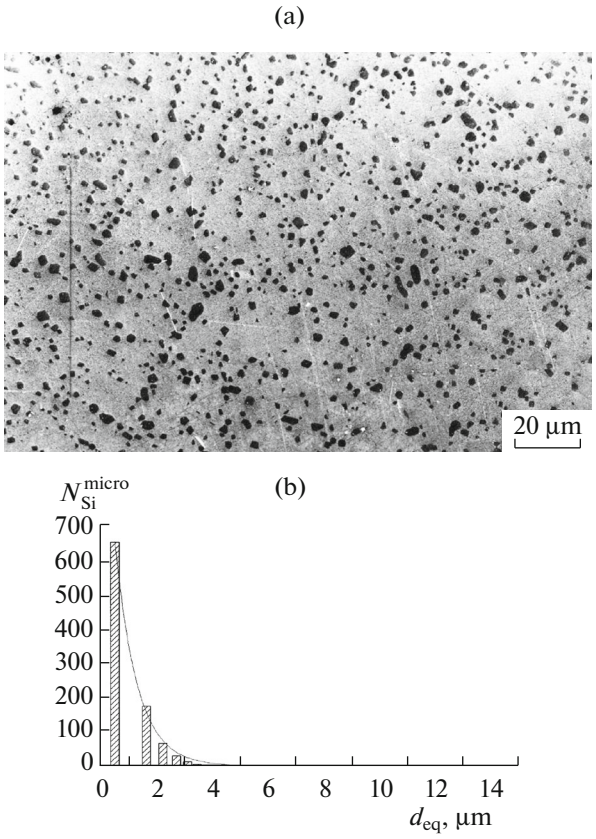

Fig. 2. (a) Microstructure of the Al–10Si alloy (SEM) produced by BTP of the Al–10Si alloy at 100 MPa and 560°C for 3 h (magnification of 2000×); (b) histogram of the size distribution of silicon microparticles in the Al–10Si alloy after BTP.

Using Eq. (1), we evaluated the diffusion distance of aluminum atoms at a temperature of 833 K and a BTP time $\tau = 10\,800$ s from the Einstein equation:

$$l_{Al/Al}^{833} = (D_{Al/Al}^{833}\tau)^{1/2}, \quad (2)$$

where $l_{Al/Al}^{833}$ (cm) is the diffusion distance of aluminum atoms, $D_{Al/Al}^{833}$ (cm^2/s) is the aluminum self-diffusion coefficient at 833 K, and τ (s) is the diffusion time. Under these conditions, the self-diffusion distance of aluminum atoms reaches 76 μm (Fig. 3, curve *1*). Therefore, the pore walls brought into contact by a plastic deformation mechanism in the aluminum matrix completely consolidate, which determines the complete density of the alloy as a result of BTP.

BTP converted the eutectic character of the silicon inclusions into a microstructure with separately arranged silicon particles. Note that the silicon particles are almost evenly distributed throughout the sample, including the dendrite axes of the primary aluminum crystals. It follows from this experimental finding that, at the isobaric–isothermal holding temperature,

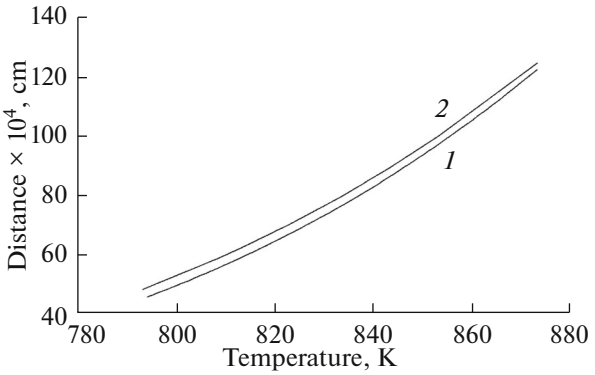

Fig. 3. Temperature dependences of (*1*) the self-diffusion distance for Al atoms and (*2*) the diffusion distance for Si atoms over a period of 3 h.

active silicon dissolution in the aluminum took place, leading to a high degree of homogenization of the alloy. In our opinion, this circumstance is due to the thermodynamically driven silicon dissolution in the aluminum under applied uniform pressure, which leads to a reduction in the lattice parameter of the aluminum-based solid solution [1] and to a reduction in its specific volume. Note that, in the case of nonequilibrium crystallization, the reduction in the lattice parameter of the aluminum may reach 5% (to a_{Al} = 4.030 Å) and the dissolved silicon concentration may exceed 10 at % [1]. An increase in silicon solubility in aluminum (up to 15 at %) at high pressures was also reported by Mii et al. [19]. Thus, as a result of barothermal processing of the Al–10Si alloy, an increased amount of silicon can dissolve in the aluminum matrix, exceeding the equilibrium value 1.38 at % in the phase diagram of the Al–Si system [1–3]. It cannot be ruled out that the entire silicon phase component of the alloy under investigation dissolves. This model is supported by the morphology of the silicon particles (Fig. 4). According to SEM data, all of the silicon microparticles have similar polyhedral morphologies, which are inherent in crystal growth at a considerable supersaturation with respect to equilibrium conditions. It follows from the SEM image in Fig. 4 that the silicon microcrystals were formed as a result of complete dissolution of the starting silicon particles upon the thermodynamically driven formation of a supersaturated (Al) solid solution during holding at 100 MPa and 560°C and its decomposition during subsequent cooling.

The silicon microcrystals are rather evenly distributed over the aluminum matrix, without predominant localization in interdendrite spaces of the primary aluminum crystals, in contrast to what is characteristic of the as-prepared alloy. To interpret this finding, we took into account the temperature dependence of the equilibrium diffusion coefficient of silicon in aluminum under

ordinary conditions [18], assuming that a uniform pressure of 100 MPa reduces it only slightly [20]:

$$D_{Si/Al} = 3.95\times10^{-4}\exp\left(-140\ \frac{\text{kJ}}{\text{mol}}\Big/RT\right), \quad (3)$$

where $D_{Si/Al}$ (m^2/s) is the diffusion coefficient of silicon in aluminum, R (J/(mol K)) is the gas constant, and T (K) is the absolute temperature.

Using relation (3) and the Einstein equation, we find that the diffusion distance during the isobaric–isothermal holding time (τ = 10800 s) at 833 K is $l^{833}_{Si/Al} = (D^{833}_{Si/Al}\tau)^{1/2}$, where $l^{833}_{Si/Al}$ (cm) is the diffusion distance of silicon atoms in aluminum, $D^{833}_{Si/Al}$ (cm^2/s) is the diffusion coefficient of silicon in aluminum at 833 K, and τ (s) is the diffusion time. Under these conditions, the diffusion distance of silicon atoms reaches 80 μm (Fig. 3, curve *2*). Therefore, the silicon atoms can be sufficiently evenly distributed over the alloy, including the dendrite axis. This model agrees well with the present SEM data (Fig. 2a).

It is seen from the histogram of the size distribution of the silicon microparticles in Fig. 2b that it is well fitted by the exponential relation

$$N^{micro}_{Si} = 1.2\times10^{3}e^{-1.3d_{eq}}, \quad (4)$$

where N^{micro}_{Si} is the number of silicon microparticles and d_{eq} (μm) is the equivalent diameter of a silicon microparticle.

The average equivalent diameter of the silicon particles was determined to be 1.6 ± 0.3 μm. Their volume fraction evaluated from the total area occupied by the silicon phase [16] was 7.7 ± 1.5 vol %. The surface and volume microparticle concentrations were 3.9×10^6 cm^{-2} and 7.7×10^9 cm^{-3}, respectively. At this surface particle concentration, the average center-to-center distance between the particles was 5.1 μm. Note that the overall content of silicon microparticles in the alloy, as determined by quantitative microstructural analysis, is lower than the nominal silicon content (10 at %). For comparison, we present quantitative data on the microstructure of the commercially available silumin AK7pch after standard heat treatment [21], in which the phase constituents at a surface density of 4.9×10^5 cm^{-2} had an average size of 5.6 μm and an average center-to-center distance of 15.6 μm. These parameters differ markedly from the quantitative characteristics of the silicon phase constituent in the Al–10Si alloy under investigation.

To obtain a more detailed information about the particle size of the silicon phase constituent, we used SEM at higher magnifications, up to 60 000× (Fig. 5). It is seen from the image in Fig. 5 that the aluminum matrix contains a considerable concentration of much finer silicon particles, ≃50–60 nm in diameter. To further ascertain this circumstance, a Si K_α X-ray map was obtained (Fig. 6). Using further data processing, we obtained an inverted-contrast image for analysis

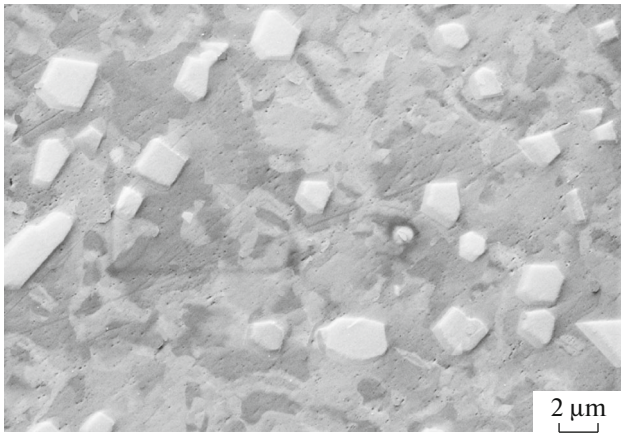

Fig. 4. SEM image of silicon microparticles in the aluminum matrix of the Al–10Si alloy after BTP (10800×).

(Fig. 6b). Note that the light areas in the normal-contrast Si K_α X-ray map corresponded to silicon particles located both in the plane of the polished section and some distance from its surface, because, in the nanometer range of particle sizes, characteristic X-rays could be generated as well by particles located in the bulk of the sample near its surface. Because of this, we found and analyzed only the brightest reflections in the image, which corresponded to the particles in the plane of the polished section. It is seen in Fig. 6b that the silicon nanoparticles are distributed nonuniformly over the aluminum matrix. Next, we obtained quantitative information about the region of the image with the maximum particle concentration (the area is delineated in Fig. 6b). A histogram of the particle size distribution for this region is displayed in Fig. 6c. The size distribution is well fitted by the exponential relation

$$N^{nano}_{Si} = 6.5\times10^{5}e^{-0.14d_{eq}}, \quad (5)$$

where N^{nano}_{Si} is the number of silicon nanoparticles and d_{eq} (nm) is the equivalent diameter of a nanoparticle.

The quantitative characteristics of the nanoscale structural constituent of the alloy were as follows: volume fraction, 2 vol %; average particle diameter, 43 nm; surface concentration, 1.4×10^9 cm^{-2}; center-to-center distance, 277 nm; volume concentration, 5.2×10^{13} cm^{-3}. It should be emphasized that the surface and volume concentrations were determined in the region with the maximum nanoparticle concentration; that is, these characteristics vary from region to region in the alloy between zero and the above values. The overall content of Si nanoparticles will then be lower than the experimentally obtained 2 vol % (≃1 vol %). The present results showing that the Al–10Si alloy contains nanoparticles correlate with findings reported by Schumacher et al. [22], who also demonstrated, using atom probe tomography, the formation of silicon nanoparticles in two hypoeutectic alloys of the Al–Si system in a solid solution region with silicon

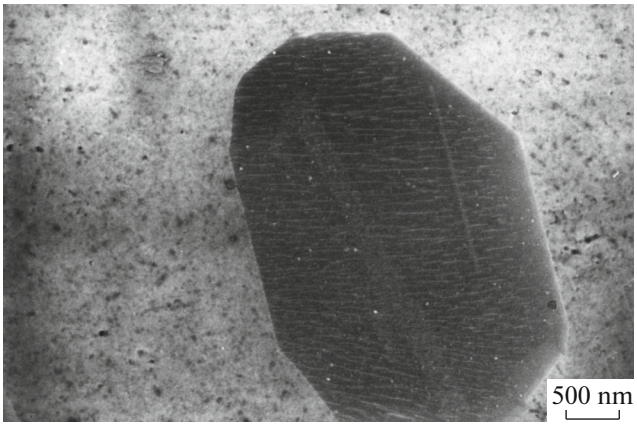

Fig. 5. Silicon nanoparticles formed in the aluminum matrix as a result of the decomposition of a supersaturated (Al) solid solution during BTP of the Al–10Si alloy (60000×).

contents below 0.72 at % in a study of silicon precipitation after annealing above the solvus temperature in the alloys at slow cooling rates (down to 0.001 K/s) under ordinary conditions.

The X-ray diffraction pattern of the Al–10Si alloy after BTP was found to contain only reflections from aluminum and silicon (Fig. 7a). The silicon content of the alloy was evaluated using the relation

$$C_{Si} = I_{Si(111)}/[I_{Si(111)} + I_{Al(111)}] \times 100, \quad (6)$$

where $I_{Si(111)}$ and $I_{Al(111)}$ are the intensities of the (111) reflections from silicon and aluminum, respectively.

Using this relation and the X-ray diffraction pattern in Fig. 7a, the overall silicon content of the Al–10Si alloy was determined to be 11.0 ± 2 at %, which corresponds to the intended silicon content. Further, based on SEM results we assumed that the silicon (111) peak was a combination of reflections from silicon microparticles and nanoparticles and that the microparticles determined primarily the intensity of the (111) peak, whereas the observed broadening of the pedestal of the peak was mainly due to the presence of silicon nanoparticles with a lower degree of structural order (Fig. 6b). The decomposition of the silicon (111) peak showed that the total composite peak could be adequately decomposed into two components differing in intensity and full width at half maximum (Fig. 7b). From these data, we found that the intensity of the small

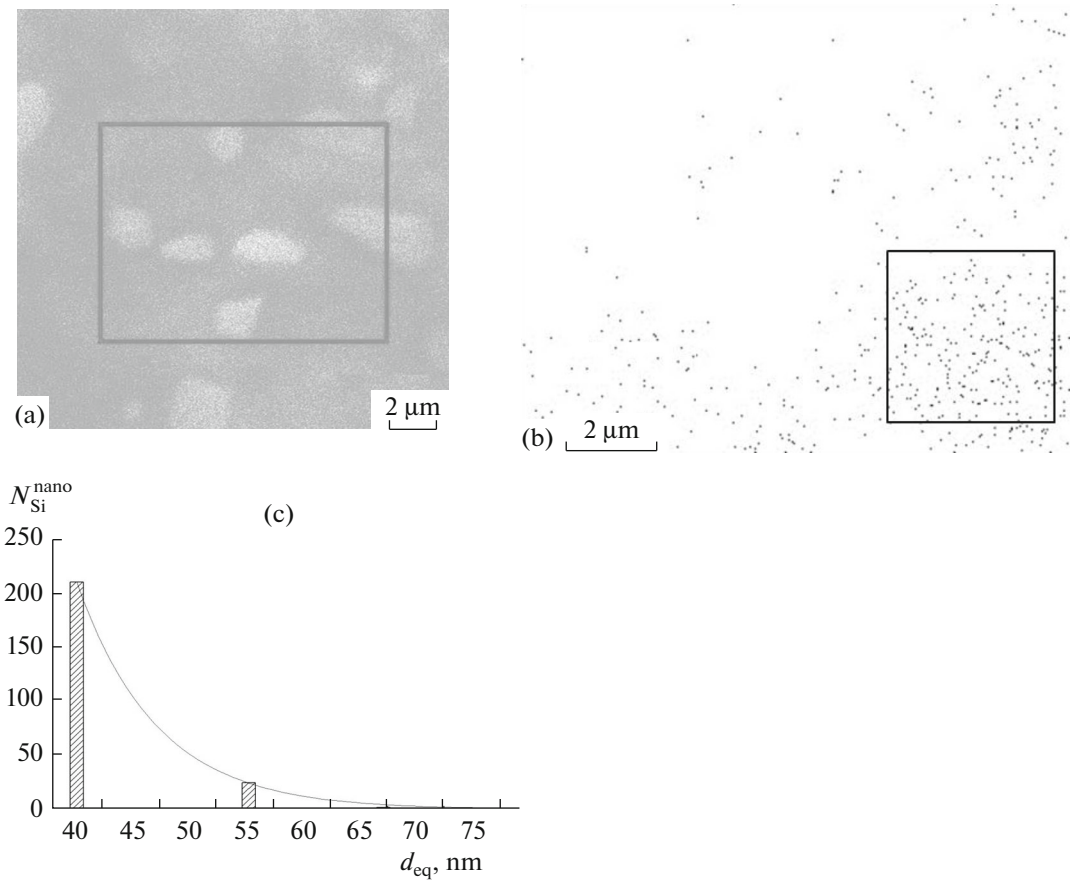

Fig. 6. Electron-microscopic examination results: (a) SEM (backscattered electron) image of the Al–10Si alloy (the outlined area was used to obtain a Si K_α X-ray map); (b) inverted-contrast Si K_α X-ray map (the outlined area was used to determine quantitative characteristics of the silicon nanoparticles); (c) semiquantitative histogram of the size distribution of the silicon nanoparticles obtained by analyzing the Si K_α X-ray map of the Al–10Si alloy.

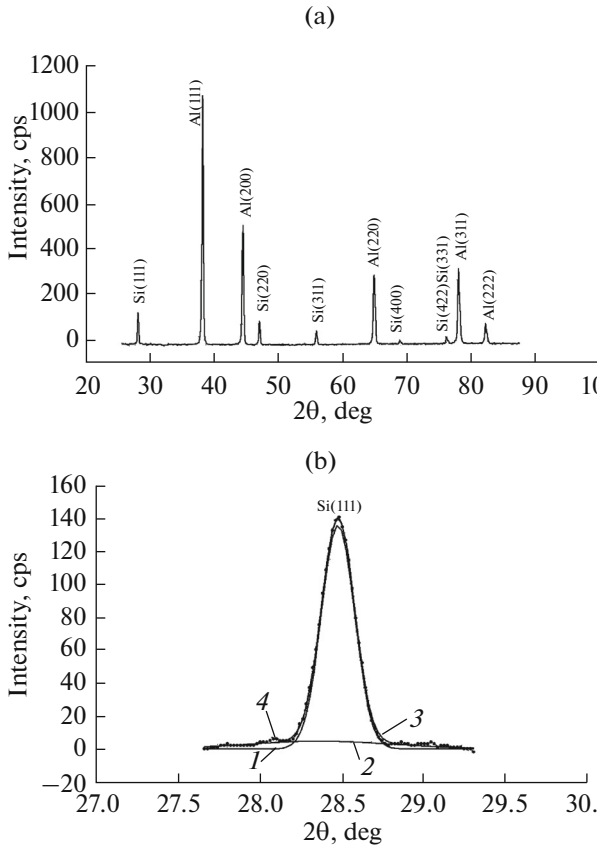

Fig. 7. X-ray diffraction characterization results: (a) X-ray diffraction pattern of the Al–10Si alloy after BTP; (b) decomposition of the Si(111) peak into (*1*) the component arising from silicon microparticles and (*2*) the component arising from silicon nanoparticles; (*3*) peak obtained as the sum of peaks *1* and *2*; (*4*) observed Si(111) peak.

peak was on the order of 3.3% of that of the main peak, which corresponded to ≃0.33 at % silicon nanoparticles in the alloy. This correlates with the insignificant heat effects of the solid-state dissolution and precipitation of silicon nanoparticles in the alloy [17] and also with the backscattered electron images and Si K_α X-ray maps obtained in this study. It follows from the decomposition parameters of the silicon (111) peak that, after BTP, the lattice parameter of the Si microparticles decreases to $a_{Si}^{micro} = 5.420 \pm 0.003$ Å, whereas the lattice parameter of the Si nanoparticles increases to $a_{Si}^{nano} = 5.443 \pm 0.003$ Å in comparison with reference data: $a_{Si} = 5.431$ Å. This dual behavior of the crystal lattices of the silicon micro- and nanoparticles can be accounted in terms of the compressive mechanical stress exerted by the aluminum matrix on the eutectic silicon crystals and also in terms of partial disordering of the crystal lattice of the nanoparticles upon precipitation from the (Al) solid solution. BTP reduces the lattice parameter of the aluminum matrix to 4.043 ± 0.003 Å (reference value $a_{Al} = 4.049$ Å), which corresponds to ≃3.8 at % silicon in aluminum in the case of

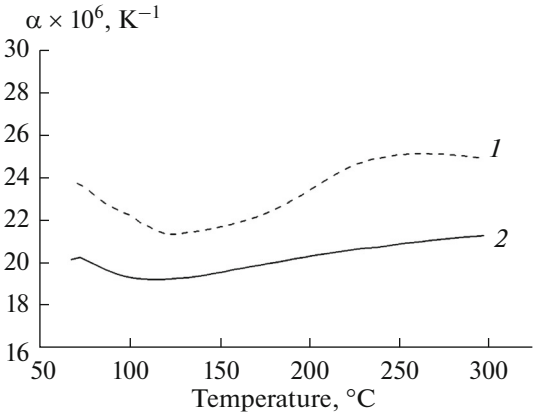

Fig. 8. TEC as a function of temperature for (*1*) the as-prepared Al–10Si alloy and (*2*) the alloy after BTP.

nonequilibrium crystallization of alloys in the Al–Si system [1].

According to thermal expansion measurements (Fig. 8), the average TEC of the as-prepared alloy (curve *1*) in the temperature range 70–150°C, $\alpha_0^{70-150} = 22.05 \times 10^{-6}$ K^{-1}, only slightly exceeds the average TEC of the heat-treated Al–10Si alloy in the temperature range 20–100°C ($\alpha_{av}^{20-100} = 21.1 \times 10^{-6}$ K^{-1}) [23]. The overestimated average TEC of the as-prepared alloy in comparison with data in the literature can be accounted for in terms of the porosity of the as-prepared alloy, in which gas-filled pores contribute to the overall increase in the length of the sample on heating on account of the increase in the internal pressure in the pores, which gives rise to additional mechanical stress in the alloy, thereby increasing its volume. A barothermal processing cycle shifts the temperature dependence of the TEC to lower values, and the average TEC in the temperature range 70–150°C decreases to a value $\alpha_{BTP}^{70-150} = 19.5 \times 10^{-6}$ K^{-1}, which is lower than that reported by Hidnert and Krider [23] (21.1×10^{-6} K^{-1}). The relative decrease in TEC is 11.6% and is determined, first, by the elimination of microporosity and an additional factor that increases thermal expansion and, second, by partial disordering of the crystal lattice of nanostructured silicon phase constituent of the alloy, which also leads to a decrease in the TEC of the alloy.

The microhardness of the alloy after BTP was determined through indentation into the two-phase material. An indent ≃800 μm^2 in area encompassed on the order of 30 silicon microparticles and up to 1×10^4 nanoparticles. The presence of silicon micro- and nanoparticles in the alloy increased the measured microhardness to 276.6 ± 11.1 MPa in comparison with pure aluminum (180–190 MPa).

CONCLUSIONS

Active diffusion processes in the Al–10Si binary alloy at a temperature of 560°C and pressure of 100 MPa make it possible to homogenize the as-prepared alloy, which is chemically and structurally inhomogeneous.

The morphology of the silicon microparticles in the Al–10Si alloy suggests that, at 560°C and a pressure of 100 MPa, all of the silicon dissolves in the aluminum matrix to form a supersaturated solid solution, which subsequently decomposes during cooling.

An applied uniform pressure of 100 MPa is many times higher than the yield strength of the alloy at 560°C and plays a key role in determining active plastic deformation of pores, closure of their walls, and subsequent diffusion joining of the surfaces brought into contact, enabling one to produce a material with 100% relative density.

BTP of the Al–10Si alloy produces a bimodal size distribution of the silicon phase constituent: microparticles 1.6 μm in average size and nanoparticles 43 nm in average size. The size distributions of the micro- and nanoparticles are well represented by exponential functions.

BTP is an effective tool for eliminating microporosity in the Al–10Si alloy, reaching a high degree of homogenization, and producing a near-optimal microstructure, which surpasses results of conventional heat treatment of the material at atmospheric and reduced pressures.

REFERENCES

1. Murray, J.L. and McAlister, A.J., The Al–Si (aluminum–silicon) system, *Bull. Alloy Phase Diagrams,* 1984, vol. 5, pp. 74–84.
2. Hansen, M. and Anderko, K., *Constitution of Binary Alloys,* New York: McGraw-Hill, 1958, 2nd ed., vols. 1–2.
3. *Diagrammy sostoyaniya dvoinykh metallicheskikh sistem* (Phase Diagrams of Binary Metallic Systems), Lyakishev, N.P., Ed., Moscow: Mashinostroenie, 1996, vols. 1–3.
4. Prigunova, A.G., Belov, N.A., Taran, Yu.N., Zolotorevskii, V.S., Napalkov, V.I., and Petrov, S.S., *Siluminy. Atlas mikrostruktur i fraktogramm promyshlennykh splavov* (Silumins: Atlas of Microstructures and Fracture Surface Maps for Industrial Alloys), Moscow: Mosk. Inst. Stali i Splavov, 1996.
5. Ceschini, L., Morri, A., and Sambogna, G., The effect of hot isostatic pressing on the fatigue behavior of sand-cast A356-T6 and A204-T6 aluminum alloys, *J. Mater. Process. Technol.,* 2008, vol. 204, pp. 231–238.
6. Chama, C.C., Distribution of Al 332 $12Fe_3Si$ and $(FeAl_6)Si$ in a hiped Al–10.71 wt % Si casting, *Mater. Charact.,* 1996, vol. 37, no. 4, pp. 177–181.
7. Garibov, G.S., Anan'ev, V.I., Koryakovtsev, A.S., and Kuz'micheva, L.G., Improving the quality of gas turbine blades from high-temperature nickel alloys by high-temperature isostatic processing, *Gazoturb. Tekhnol.,* 2004, no. 8, pp. 14–16.
8. Barinov, S.M., Ponomarev, V.F., Shevchenko, V.Ja., and Skawran, D., Effect of post-hot isostatic pressing on mechanical properties of zirconia-toughened alumina, *J. Mater. Sci. Lett.,* 1995, vol. 14, pp. 871–872.
9. Bouvard, D. and Ouedraogo, E., Modeling of hot isostatic pressing: a new formulation using random variables, *Acta Metall.,* 1987, vol. 35, no. 7, pp. 2323–2328.
10. Li, E.K.H. and Funkenbusch, P.D., Modeling of the densification rates of monosized and bimodal-sized particle systems during hot isostatic pressing (HIP), *Acta Metall.,* 1989, vol. 37, no. 6, pp. 1645–1655.
11. Nair, S.V. and Tien, J.K., Densification mechanism map for hot isostatic pressing (HIP) of unequal sized particles, *Metall. Trans. A,* 1987, vol. 18, no. 1, pp. 97–107.
12. Li, W.-B., Ashby, M.F., and Easterling, K.E., On densification and shape change during hot isostatic pressing, *Acta Metall.,* 1987, vol. 35, no. 12, pp. 2831–2842.
13. Wadley, H.N.G., Schaefer, R.J., Kahn, A.H., Ashby, M.F., Clough, R.B., Geffen, Y., and Wlassich, J.J., Sensing and modeling of the hot isostatic pressing of copper pressing, *Acta Metall. Mater.,* 1991, vol. 39, no. 5, pp. 979–986.
14. Shrinivasan, R. and Weiss, I., Formation of surface depressions during hot isostatic pressing (HIP), *Scr. Metall. Mater.,* 1990, vol. 24, pp. 2413–2418.
15. Zulfia, A., Atkinson, H.V., Jones, H., and King, S., Effect of hot isostatic pressing on cast A357 aluminum alloy with and without SiC particle reinforcement, *J. Mater. Sci.,* 1999, vol. 34, pp. 4305–4310.
16. Saltykov, S.A., *Stereometricheskaya metallografiya* (Stereometric Metallography), Moscow: Metallurgiya, 1976.
17. Padalko, A.G., Akopyan, T.K., Dedyaeva, E.V., Talanova, G.V., Shvorneva, L.I., Zubarev, G.I., Fedotov, V.T., and Suchkov, A.N., Phase transformations in a binary 10 at % Si–90 at % Al alloy at high pressures and temperatures, *Russ. Metall.* (Engl. Transl.), 2014, no. 5, pp. 361–366.
18. Fujikawa, S.-I., Hirano, K.-I., and Fukushima, Y., Diffusion of silicon in aluminum, *Metall. Trans. A,* 1978, vol. 9, pp. 1811–1815.
19. Mii, H., Senoo, M., and Fujishiro, I., Solid solubility of Si in Al under high pressure, *Jpn. J. Appl. Phys.,* 1976, vol. 15, pp. 777–783.
20. Beresnev, A.G., Razumovskii, I.M., Marinin, S.F., Tikhonov, A.A., and Butrim, V.N., Technological principles underlying the hot isostatic pressing of monocrystalline blades from high-temperature nickel alloys for aero engines, *Tsvetn. Met.,* 2011, no. 12, pp. 84–88.
21. Belov, N.A., *Fazovyi sostav promyshlennykh i perspektivnykh alyuminievykh splavov* (Phase Composition of Commercially Available and Promising Aluminum Alloys), Moscow: Izd. Dom Mosk. Inst. Stali i Splavov, 2010.
22. Schumacher, P., Reich, M., Mohles, V., Pogatscher, S., Uggowitzer, P.J., and Milkereit, B., Correlation between supersaturation of solid solution and mechanical behaviour of two binary Al–Si-alloys, *Mater. Sci. Forum,* 2014, vols. 794–796, pp. 508–514.
23. Hidnert, P. and Krider, H.S., Thermal expansion of aluminum and some aluminum alloys, *J. Res. Natl. Bur. Stand.,* 1952, vol. 48, no. 3, pp. 209–220.

Translated by O. Tsarev